Measurement of three-dimensional welding torch orientation for manual arc welding process

2014 Meas. Sci. Technol. 25 035010

(http://iopscience.iop.org/0957-0233/25/3/035010)

IOP Publishing Measurement Science and Technology
Meas. Sci. Technol. **25** (2014) 035010 (17pp) doi:10.1088/0957-0233/25/3/035010

Measurement of three-dimensional welding torch orientation for manual arc welding process

Weijie Zhang[1], **Jun Xiao**[1,2], **HePing Chen**[3] **and YuMing Zhang**[1]

[1] Department of Electrical and Computer Engineering and Institute for Sustainable Manufacturing, University of Kentucky, Lexington, KY 40506, USA
[2] National Key Lab of Advanced Welding and Joining in Harbin Institute of Technology, Harbin, 150001, People's Republic of China
[3] Ingram School of Engineering, Texas State University–San Marcos, 601 University Drive, San Marcos, TX 78666, USA

E-mail: ymzhang@engr.uky.edu

Received 19 August 2013, revised 27 November 2013
Accepted for publication 6 January 2014
Published 17 February 2014

Abstract

Torch orientation plays an important role in welding quality control for a manual arc welding process. The detection of the torch orientation can facilitate weld monitoring, welder training, and may also open a door to many other interesting and useful applications. Yet, little research has been done in measuring the torch orientation in the manual arc welding process. This paper introduces a torch orientation measurement scheme that can be conveniently incorporated both in a real manual arc welding process and in a welder training system. The proposed measurement employs a miniature wireless inertial measurement unit (WIMU), which includes a tri-axial accelerometer and a tri-axial gyroscope. A quaternion-based unscented Kalman filter (UKF) has been designed to estimate the three-dimensional (3D) torch orientation, in which the quaternion associated with the orientation is included in the state vector, as is the angular rate measured by the gyroscope. In addition, an auto-nulling procedure has been developed where the WIMU drift and measurement noise are captured and adaptively compensated in-line to ensure the measurement accuracy. The performance of the proposed scheme has been evaluated by simulations and welding experiments with different types of processes and fit-ups. The simulation results show that the inclination (x- and y-axes) of the torch has been accurately measured with a root-mean-square error (RMSE) in the order of 0.3°. The major error obtained in the heading (z-axis) measurement has been reduced significantly by the proposed auto-nulling procedure. Statistics from welding experiments indicate the proposed scheme is able to provide a complete 3D orientation measurement with the RMSE in the order of 3°.

Keywords: welding torch orientation, auto-nulling, unscented Kalman filter, quaternion

(Some figures may appear in colour only in the online journal)

1. Introduction

Arc welding has been developed and refined for years, as one of the most widely used material joining technologies. High-quality welds are critical for many applications, such as automobile manufacturing, refineries and ship building. The torch orientation is defined as the torch posture throughout a welding process. It is one of the most important welding parameters, and is directly contingent upon the weld quality and appearance. Optimal quality welds can only be guaranteed if the torch orientation is well adjusted. Inappropriate torch manipulations cause various weld defects and discontinuities,

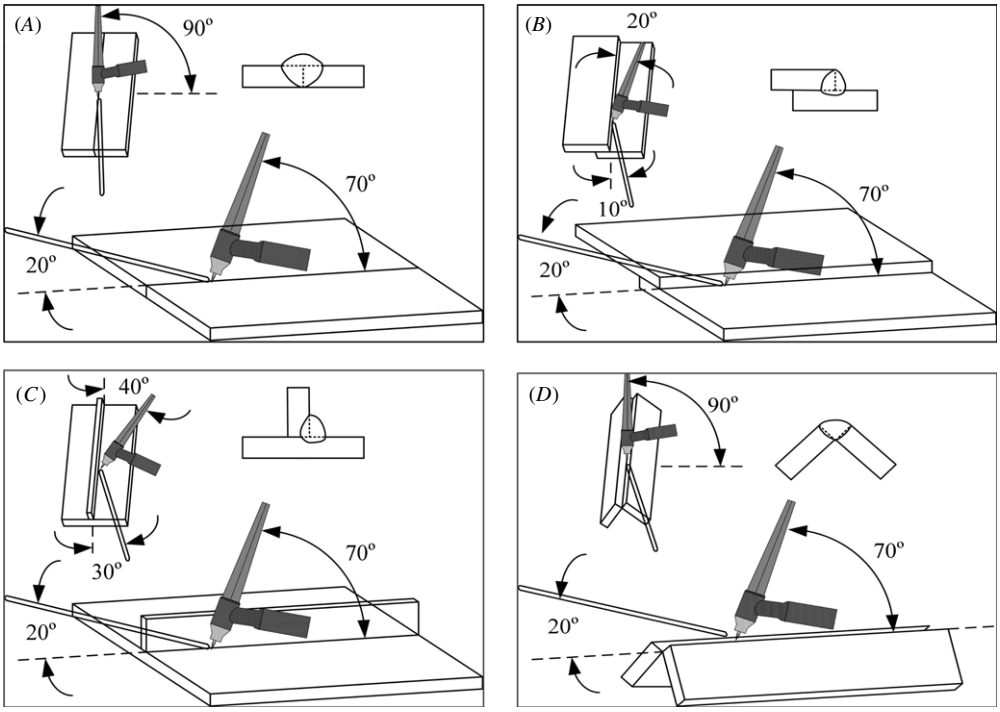

Figure 1. Torch orientations for different weld types in the GTAW process: (*A*) butt welds; (*B*) lap joint; (*C*) T-joint; and (*D*) corner joint.

such as poor penetration, undercuts, porosity and different types of cracks [1–3]. Therefore, detailed torch orientations for almost every welding process have been recommended by both standardization organizations such as the American Welding Society (AWS) [4, 5] and by different welding-related companies [6–8].

Different welding processes may have various parameters such as the welding current, voltage, torch traveling speed, wire feed speed if applicable and the number of weld passes per layer. The recommended torch orientation manipulations can differ accordingly. Typical recommended torch postures are shown in figures 1 and 2 for the two welding processes: gas tungsten arc welding (GTAW) [9] and gas metal arc welding (GMAW) [7], respectively. Four different fit-up types for each process are illustrated in the two figures. Moreover, four different torch swing patterns are adopted for the four fit-up types in figure 2, besides the diversities in torch orientation.

Mastering the torch manipulation is challenging in a manual arc welding process. To ensure weld quality, a human welder is required to maintain a recommended torch posture while moving the torch smoothly along the weld bead, possibly with one particular swing pattern. Due to various disturbances in the welding field, the torch is required to be adjusted accordingly to guard against the effects of the disturbances to the weld quality. The capability of proper torch orientation manipulation depends on the welder's skill level and his/her physiological conditions [10]. The major problem is that a welder cannot master the torch adjusting maneuver without countless hours of practice through acquired rule-of-thumb techniques, and this makes the welder training cycle intolerably long.

Torch orientation measurement can be used to accelerate the welding training process. A database of welding experts' performance can be established using the torch manipulation data combined with other critical welding parameters. With the database, the operations of a welding trainee can be compared with the expert's performance throughout the practice by detecting the torch orientation in real-time, and incorrect or unfavorable operations from the trainee can be identified immediately. Audio or visual indications can thus be provided to the trainee as instant performance feedback throughout the training practice [11, 12]. It was found that welding skills were increased significantly with this feedback [12].

Detecting the torch manipulation may also open the door to better understanding of the intelligent welding operations of skilled welders. Given that a skilled welder's torch maneuvers are detected, the dynamics of the torch orientation related to the weld quality control can be obtained [13]. The mathematical formulation of the experts' welding skills, which make an experienced welder better than a unskilled welder in delivering quality weld, can be further established [14]. Applying the formulated skill to automatic welding will build the foundation for the next generation of intelligent welding robots that possess disturbance-resistant capabilities comparable to a skilled human welder.

This study aims to develop an accurate three-dimensional (3D) torch orientation measurement scheme that can be conveniently used in a real manual arc welding process or a welder training system. Based on a miniature wireless inertial measurement unit (WIMU), the proposed scheme consists of a quaternion-based unscented Kalman filter (UKF) and an auto-nulling algorithm. The UKF is designed to estimate the 3D orientation with the rotation quaternion included in its state vector. The innovative auto-nulling algorithm captures and compensates the gyro drift based on the gyro's own

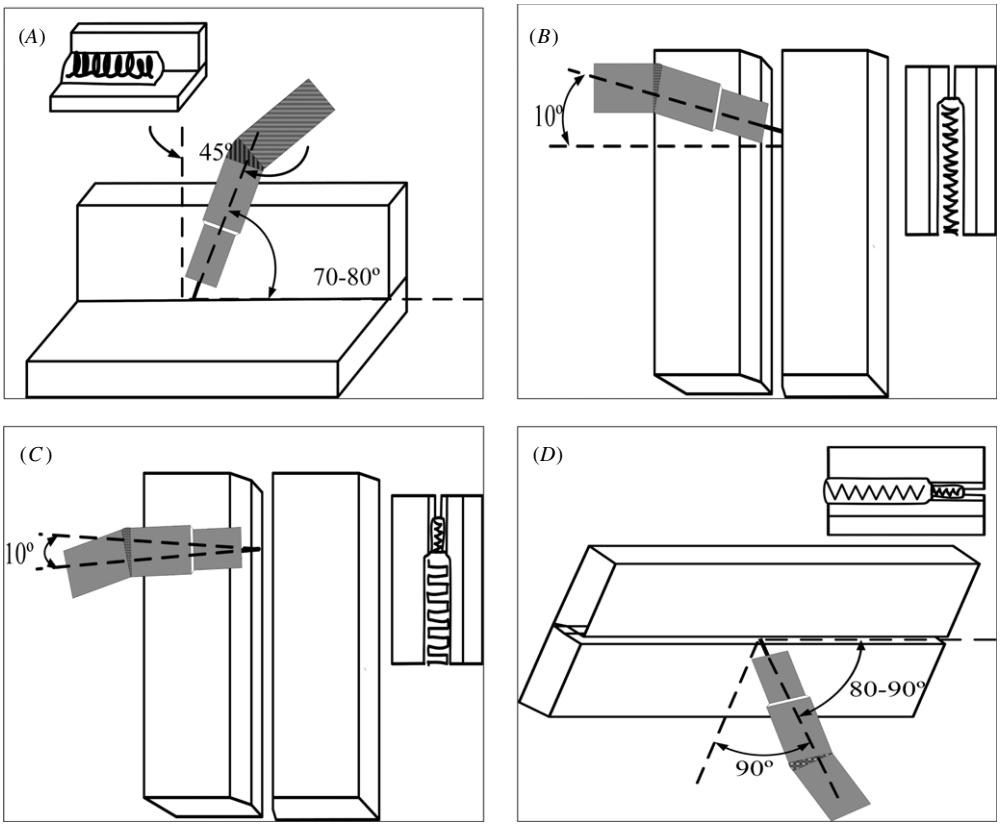

Figure 2. Torch orientations for different weld types in non- and low-alloyed steel in the GMAW process: (*A*) 2F/PB-horizontal–vertical fillet; (*B*) 3G↑/PF-vertical up root pass and (*C*) fill passes; and (*D*) 4G/PE-overhead.

output, unlike most other drift compensation algorithms, which require extra information from an accelerometer. The proposed UKF incorporated with the auto-nulling algorithm provides a complete 3D estimation with a reasonable accuracy, without the aid of a magnetometer—a feature that is lacking in most orientation filters the authors are aware of. Moreover, this paper is the first of this kind to measure the 3D welding torch orientation. The detection of human welders' torch manipulation is the foundation of studying their experienced behavior during the arc welding process, which has been extensively studied by the authors [13–16]. It is the core to understanding the difference between skilled and unskilled welders and can be utilized in accelerating the welder training process and developing next generation of intelligent welding robots. By simulations and experimental validation with torch motion signals captured from the real arc welding process, improvements in the accuracy of orientation estimation are demonstrated as compared with other orientation estimation counterparts.

2. Related works

Within the scope of the authors' limited searching capability, there is no literature found that studies welding torch orientation sensing in a manual arc welding process. A number of previous researchers focused on welding position sensing in robotic welding [17–21]. However, those studies addressed the spatial position of the tungsten tip (in GTAW) or the wire tip (in GMAW) relative to a visual reference (e.g., a laser marker), indicating the location of a weld seam. No torch orientation detection was involved, while this study concentrates on the 3D orientation of the torch throughout a manual arc welding process. In [22], a speed and position sensor was proposed based on an accelerometer for a manual plasma pipe welding process in pulse current mode. Yet, the comparatively rigid assumptions on the torch movement pattern constrict its application in the other fit-ups (flat butt joint, T-type, etc) or power modes (constant current, constant voltage, etc).

Torch posture detection is essential in welder training systems. However, those orientation detection technologies constrict themselves in certain working circumstances due to their own inherent constraints. For example, in the welding simulator SimWelder from VRsim, Inc, the angular orientation of the welding torch is tracked using a tri-axial measurement gimbal at the attachment of the torch to the haptic device [23]. Yet, the hulking measurement device cannot be augmented to a torch in a real welding process. For the RealWeld Trainer, the torch posture is measured by detecting the spatial position of an infrared target mounted on the torch using three cameras augmented on the simulator stand [24]. The 2D torch orientation was measured using a tri-axial accelerometer in the computer-based welder training system in [12]. However, the variation of the torch orientation in the gravitational direction cannot be detected. There are also several virtual-reality-based welder training systems augmented with 2D

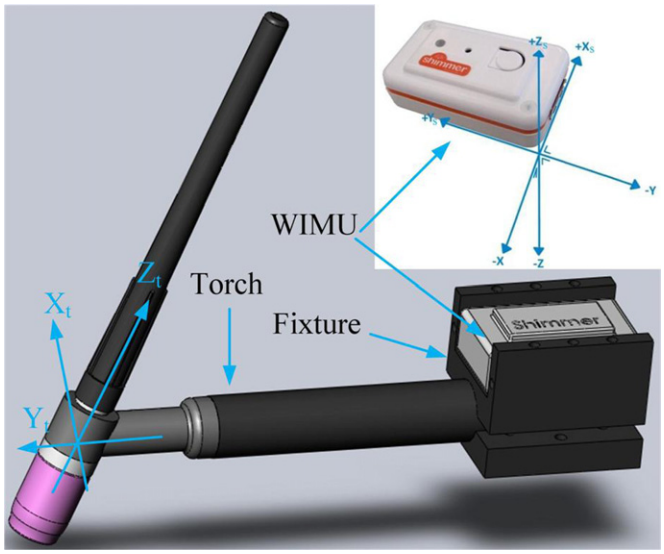

Figure 3. An illustration of the torch and WIMU, which is rigidly amounted on the torch handle by a hard plastic fixture. ${}^{t}(XYZ)$ and ${}^{s}(XYZ)$ denote the 3D Cartesian coordinate system for the torch and the WIMU, respectively.

torch posture measurements, the accuracy of which is yet undisclosed [11, 25].

Accurate orientation measurements have been intensively investigated in a range of fields including avionics [26, 27], navigation [28, 29], human motion analysis [30, 31] and robotics [32]. Within a variety of technologies capable of orientation measurement, inertial sensing has the advantage of being smaller, cheaper, internally referenced and immune to constraints in any motion or specific environment [33, 34]. An IMU (inertial measurement unit) normally consists of an accelerometer and a gyroscope. It is capable of detecting the acceleration and the angular velocity of a rigid body on which the unit is attached. A tri-axial accelerometer can be used as an inclinometer when the magnitude of the detected acceleration can be neglected with respect to the gravitational direction [35]. However, the accelerometer signal does not contain information for the rotation along the gravitational direction. Changes in orientation can be estimated by integrating the angular velocity measured by a gyroscope [36, 37]. The problem is that time-integrating the gyro signals superimposed with sensor drift and noise leads to an unbounded estimation error.

Recent research has been carried out to develop different filters using both the gyroscope and the accelerometer to estimate the orientation of a rigid body [38]. The orientation error resulting from the gyro output drift can be mitigated by additional sensors, the information from which is able to correct the orientation errors. The traditional use of a linear Kalman filter (KF) and its extended version (EKF) for nonlinear models has been well established for orientation estimation [30, 32, 35, 39] and commercial inertial orientation sensors [40–42]. Both the gyro data and acceleration data are applied in the KF or EKF based estimation algorithms.

For an accurate heading estimation, extra data from an additional magnetometer was incorporated in the Kalman filter-based algorithms [43, 44]. The adaptive EKF developed in [43] and [45] was embedded in an IMU incorporated with an magnetometer. The angular position was calculated mainly by the gyro data; the accelerometer was used to estimate the inclination; and the magnetometer was used to estimate the heading angle. However, the use of the magnetometer could give large errors in the vicinity of a strong magnetic field, especially in places like the welding field where the welding machine and the welding arc are the sources of an extremely strong, time-varying, electromagnetic field [46]. Although a Kalman filter was proposed in [47] with a magnetic disturbance resistance to some extent, the designed magnetic disturbance, caused by an iron cylinder, was much smaller compared to the disturbance caused by a welding machine/arc [48, 49]. Therefore, the WIMU in this study precludes the employment of an electromagnetic field for torch orientation estimation. An auto-nulling algorithm is proposed to compensate for the drift and measurement noise from the gyroscope, to ensure the accuracy of the heading estimation for the welding torch.

In addition, a quaternion was employed to represent the angular position since it requires less time complexity and avoids the singularity problems [50]. The attitude or orientation determination algorithm was developed in [51–53] based on the UKF instead of the traditional KF or the EKF, since the UKF is thought by many to be more accurate and less time complex [54, 55].

3. Experimental system

The WIMU (a Shimmer motion sensor) used here is shown in figure 3. The size of the WIMU is about 53 mm $\times$32 mm $\times$19 mm. It is an IMU with wireless capability which is composed of a tri-axial accelerometer (Freescale MMA7260Q), a tri-axial gyro sensor (InvenSense 500 series), a microprocessor (MSP430F1611), and a Bluetooth unit. The accelerometer is endowed with one filter capacitor in each axis. The gyro sensor contains three vibrating elements. The angular rate at each axis is obtained by measuring the Coriolis acceleration of the corresponding vibrating elements. The microprocessor captures the sensor data using a 12-bit analogue-to-digital converter (ADC) at a pre-defined frequency. The Bluetooth unit transmits the data from the WIMU to a desktop. The calibration procedure for the sensors is performed according to literature [56].

A torch for the GTAW process with the attached WIMU is illustrated in figure 3. The WIMU is mounted rigidly at the tail of the torch using a plastic fixture. The 3D Cartesian coordinate frame, denoted as ${}^{s}(XYZ)$, in the WIMU is its internal frame. It is worth noting that during the assembly process, the torch was first held still such that its handle was perpendicular to the gravitation direction, with aid from external calibration tools, such as a gravimeter; the WIMU was installed such that the gravitational acceleration direction coincided with the ${}^{s}Z$ axis. The coordinate frame ${}^{t}(XYZ)$ is the internal frame for the torch. It is defined in the following manner: axis ${}^{t}Z$ coincides with the torch head direction, axis ${}^{t}X$ coincides with axis${}^{s}X$. By doing this, frame ${}^{t}(XYZ)$ can be obtained by rotating frame ${}^{s}(XYZ)$ around the ${}^{s}X$ axis for an angle denoted as θ_{st}.

4. Method

4.1. Orientation representation

The orientation of the torch is determined when the axis orientation of the coordinate frame ${}^{t}(XYZ)$ is obtained with respect to an absolute 3D Cartesian coordinate frame, denoted as frame ${}^{\mathsf{E}}(XYZ)$. The negative direction of axis ${}^{\mathsf{E}}Z$ is defined in coincidence with the local gravitational direction. The directions of the other two axes depend on the specific welding applications, which will be detailed in section 5.

The torch orientation is presented by a quaternion denoted as ${}^{s}_{E}\tilde{q}$, where the sign $\tilde{}$ denotes a unit quaternion $\tilde{q} = [q_0, q_1, q_2, q_3]$, i.e.,[4]

$$\|\tilde{q}\| = \sqrt{q_0^2 + q_1^2 + q_2^2 + q_3^2} = 1 \tag{1}$$

where q_0 is the scalar part and $[q_1, q_2, q_3]$ is the vectorial part of the quaternion.

The tri-axial gyroscope in the WIMU measures the angular velocity of frame ${}^{s}(XYZ)$ relative to frame ${}^{\mathsf{E}}(XYZ)$. The measurement (in rad s^{-1}) can be denoted by the 1×3 row vector shown in equation (2):

$${}^{s}\omega = [\omega_x, \omega_y, \omega_z]. \tag{2}$$

The quaternion at instant $k+1$ can be presented using the quaternion at instant k, angular measurement (${}^{s}\omega_k$), and the time interval denoted by T_s [50]:

$${}^{s}_{E}\tilde{q}_{k+1} = {}^{s}_{E}\tilde{q}_k \otimes \exp\left(\frac{T_s}{2}\omega_k\right) \tag{3}$$

where $\otimes$ is the quaternion product, which is defined in equation (4), where $a = [a_1 \quad a_2 \quad a_3 \quad a_4]$ and $b = [b_1 \quad b_2 \quad b_3 \quad b_4]$. $\mathrm{Exp}(\cdot)$ denotes the quaternion exponential, which is defined in equation (5).

$$a \otimes b = \begin{bmatrix} a_1b_1 - a_2b_2 - a_3b_3 - a_4b_4 \\ a_1b_2 + a_2b_1 + a_3b_4 - a_4b_3 \\ a_1b_3 - a_2b_4 + a_3b_1 + a_4b_2 \\ a_1b_4 + a_2b_3 - a_3b_2 + a_4b_1 \end{bmatrix}^{T} \tag{4}$$

$$\exp(v) \triangleq \left[\cos(\|v\|), \frac{v}{\|v\|}\sin(\|v\|)\right] \tag{5}$$

where v presents a 1×3 row vector. The torch orientation, ${}^{t}_{E}\tilde{q}$, can be calculated by equation (6):

$${}^{t}_{E}\tilde{q} = {}^{s}_{E}\tilde{q} \otimes \exp([\theta_{st}, 0, 0]). \tag{6}$$

4.2. Sensor model

The gyroscope and the accelerometer in the WIMU measure the angular velocity and the acceleration of the sensor, respectively. Besides the true values, ${}^{s}\omega_{\mathrm{true}}$ and ${}^{s}a_{\mathrm{true}}$, there are several main error sources affecting the WIMU measurement including the bias, scale-factor instability, non-orthogonality of axes and the measurement noise. To this regard, the WIMU measurements are expressed in equations (7) and (8):

$${}^{s}\omega = S_\omega {}^{s}\omega_{\mathrm{true}} + T_\omega {}^{s}\omega_{\mathrm{true}} + b_\omega + v_\omega \tag{7}$$

$${}^{s}a = S_a {}^{s}a_{\mathrm{true}} + T_a {}^{s}a_{\mathrm{true}} + b_a + v_a \tag{8}$$

where S_ω and S_a are the scale-factor matrices; T_ω and T_a are the non-orthogonality factor matrices; b_ω and b_a are the bias; and v_ω and v_a are the measurement noises. Please note this is a simplified sensor model. Some minor error sources are not considered, such as the cross-sensitivity and gravity-sensitivity.

Measurement noises v_ω and v_a are normally considered as uncorrelated white Gaussian noises, with a null mean and 3×3 covariance matrices ${}^{R}\sigma_\omega^2\mathbf{I}_{3\times3}$ and ${}^{R}\sigma_a^2\mathbf{I}_{3\times3}$, respectively. The covariance matrix of sensor model R is

$$R = \begin{bmatrix} {}^{R}\sigma_\omega^2\mathbf{I}_{3\times3} & \mathbf{0} \\ \mathbf{0} & {}^{R}\sigma_a^2\mathbf{I}_{3\times3} \end{bmatrix}. \tag{9}$$

The true acceleration measurement includes two components: the sensor acceleration and the gravitation acceleration, as expressed by equation (10):

$${}^{s}a_{\mathrm{true}} = {}^{s}a_{\mathrm{sensor}} + {}^{s}g \tag{10}$$

where ${}^{s}g$ is the gravitational acceleration in the sensor frame, which can be obtained using equation (11):

$${}^{s}g = {}^{s}_{E}\tilde{q} \otimes [0, {}^{E}g] \otimes {}^{s}_{E}\tilde{q}^{*}. \tag{11}$$

The torch should be moved smoothly along the weld bead with unnoticeable accelerations or decelerations throughout the arc welding process, given that the skilled welder is well motivated. Thereby, ${}^{s}a_{\mathrm{sensor}}$ is insignificant compared with the gravitation acceleration and thus is considered as a disturbance in our application. Henceforth, equation (10) can be expressed by equation (12):

$${}^{s}\tilde{a}_{\mathrm{true}} \cong {}^{s}\tilde{g}. \tag{12}$$

Using normalized gravity can eliminate the measurement error caused by localized gravity differences.

The bias and the scale factors, in equations (7) and (8), depend on the sensors' imperfections and the working field. The typical gyro bias is 0.017–0.17 rad h^{-1} and the acceleration bias is about 100–1000 μg for tactical grade [57]. In particular, the ambient temperature significantly affects the gyro's bias. In this study, the WIMU is employed near the welding arc which is a strong heat source. Hence, the gyro bias might not be constant throughout an arc welding process. To this regard, an auto-nulling algorithm is proposed to compensate the gyro's drift in-line to guard the effect of the drift variation over temperature to the estimation accuracy.

The influence of temperature on the accelerometer's bias is much less intense. The in-line calibration of an accelerometer usually requires the accelerometer to remain in a static or quasi-static condition for several different orientations [58]. However, in our application, the torch should be held in one certain orientation, as shown in figures 1 and 2, throughout the arc welding process. Therefore, there will not be enough orientations for in-line calibration. In this study, the accelerometer bias is assumed to be constant, and can be compensated for by calibration before use [56].

The scale-factor drifts of WIMU are known to affect the measurement accuracy to a much smaller extent than the bias drifts. The drift variation over temperature is also

[4] For the quaternion denotation, a leading subscript denotes the reference frame and a leading superscript indicates the frame being described.

negligible [59]. Therefore, the scale factors can be considered to be subjected to small variations around their average values throughout the welding process. Their nominal values can be determined through the sensor calibration before use [56].

4.3. Auto-nulling algorithm for gyro sensor drift

The capture of the gyro drift usually requires keeping the gyro sensor from rotation. The basic principle is called the zero attitude update (ZAU), also referred as auto-nulling, i.e., when no rotation occurs to the gyro sensor, its output can be considered as the drift caused by the bias and other error sources. The drift can then be periodically captured and compensated for. A ZAU algorithm was proposed in [60] to detect the human walking pace. The static status (i.e. no rotation) of the gyro sensor was detected by an accelerometer. However, that ZAU algorithm is only valid in 2D applications since the accelerometer cannot detect the gyro's rotation in the gravitational direction. In [61], the authors compensated for the gyro drift using an off-line ZAU algorithm in a gait pace detection application. The starting and ending time of a gait period were required before the gyro data recorded within the period was processed. Effective drift estimation was also accomplished by using an extra Kalman filter [62]. Yet, introducing an additional Kalman filter to estimate the gyro drift in our application is not computation efficient. Therefore, a new auto-nulling algorithm is proposed in this study in which the static status is detected using information from the gyro's own output.

The mean and deviation of the gyro's output obtained in a small time interval when the WIMU is set still can be used to determine the static status. The two variables are defined by

$$\mu_s = \sum_{k=1}^{M} {}^s\omega_k / M \tag{13}$$

and

$$\sigma_s = \sqrt{\frac{\sum_{k=1}^{M} ({}^s\omega_k - \mu_s) * ({}^s\omega_k - \mu_s)'}{M}} \tag{14}$$

where M is the number of samples. To record the data for calculating μ_s and σ_s, a static state experiment was conducted where the WIMU was set still at room temperature (about 23 °C). Before recording valid gyro data, the WIMU was allowed to power up for a few minutes until it reached thermal stability.

For an arbitrary angular velocity ${}^s\omega_i$ recorded by the gyro sensor, the corresponding mean and deviation are defined in equations (15) and (16)

$$\mu(i) = \sum_{k=i-N}^{i} {}^s\omega_k / N \tag{15}$$

$$\sigma(i) = \sqrt{\frac{\sum_{k=i-N}^{i} ({}^s\omega_k - \mu(i)) * ({}^s\omega_k - \mu(i))'}{N}} \tag{16}$$

where $i > N$, and N is the sampling number gathered in a small interval T_{au} right before ${}^s\omega_i$ is recorded. In this study, $T_{au} = 1$ s.

If the mean and the deviation of the gyro output within the interval T_{au} are close to μ_s and σ_s, then the torch/WIMU is considered to be in the static state. According to the ZAU principle, the mean value, $\mu(i)$, can be thus thought of as a drift. In our application, the possible ambient temperature variation caused by the welding arc should be in a comparatively low rate due to the thermal latency. Therefore, the gyro data in the time vicinity of the static interval can be compensated using the drift obtained in the stationary interval. If the WIMU is in a dynamic period ($\mu(i)$ or $\sigma(i)$ are much larger than μ_s and σ_s), then compensation can be accomplished by the mean value from the nearest static interval.

Furthermore, the drift of a gyro sensor is sensitive to temperature, as discussed in the last section. Therefore, two thermal coefficients are included in the auto-nulling algorithm, ρ_μ and ρ_σ, accounting for the temperature difference between the environment where the torch/WIMU is used and the one where the static experiment was conducted. For the simulations in section 5, they were set 1, since the temperature at which the static experiment was conducted was about the same as that in which the simulations were conducted. In the welding experiments, they were pre-set and given reasonable values based on estimation results. In practical applications, the two coefficients can be empirically chosen.

Hence, if there exist

$$\mu(i)^2 \leqslant \rho_\mu \mu_s^2 \quad \text{and} \quad \sigma(i) \leqslant \rho_\sigma \sigma_s \tag{17}$$

then the torch/WIMU is considered to be in stationary state, and $\mu(i)$ is referred to as a valid drift.

Therefore, the proposed auto-nulling algorithm can be expressed by

$${}^s\omega_i = \begin{cases} {}^s\omega_i - \mu_s & i \leqslant N \\ {}^s\omega_i - \mu(i) & \text{WIMU is static}, i > N \\ {}^s\omega_i - \mu(\xi) & \text{WIMU is dynamic}, i > N \end{cases} \tag{18}$$

where $\mu(\xi)$ is the nearest valid drift for ${}^s\omega_i$, $\xi < i$.

Using the proposed auto-nulling algorithm, no data is required from some external sensors to compensate for the effect of drift to the orientation estimation. The effectiveness of the algorithm will be evaluated in section 6.

4.4. Filter design

The state vector of the proposed UKF is composed of the torch orientation quaternion and the angular velocity.

$$x_k = \left[{}^s_E\tilde{q}_k, {}^s\omega_k\right]. \tag{19}$$

Using the state vector, the sensor model (equations (7) and (8)) can be rewritten as shown in equation (20):

$$z_{k+1} = h(x_k, v_k) \tag{20}$$

where $z_{k+1} = [{}^s\omega_{k+1}, {}^s a_{k+1}]$, and $v_k = [v_\omega, v_a]$.

The process model represented by the state vector is

$$x_{k+1} = f(x_k, w_k) = \left[{}^s_E\tilde{q}_k \otimes \exp(\omega_k) \otimes \exp(w_q), {}^s\omega_k + w_\omega\right] \tag{21}$$

where $w_k = [w_q, w_\omega]$ is the process noise with a covariance matrix denoted as Q_k, $\exp(\omega_k)$ is the increment of the rotation in the kth sampling period, and $\exp(w_q)$ is the process

uncertainty caused by w_q, which is the quaternion component of the process noise.

In this study, the angular velocity is expected to be fairly small, since the torch is required to be maintained in a recommended orientation with small adjustments for possible disturbances. Therefore, the angular velocity can be modeled as a random walk in the process model.

Because of the nonlinear nature of the process model (equation (21)) and the sensor model, the UKF approach is applied [54]. For the sake of readers' convenience, the UKF algorithm is summarized below.

Given the estimated state vector $\hat{x}_{k-1}$ and its covariance P_{k-1} at instant $k-1$, an auxiliary vector set $\{\psi_i\}$ is defined by equation (22):

$$\psi_i = \begin{cases} (\sqrt{(n+\lambda)\cdot(P_{k-1}+Q)})_i & i = 1,\ldots,n \\ -(\sqrt{(n+\lambda)\cdot(P_{k-1}+Q)})_{(i-n)} & i = n+1,\ldots,2n \end{cases} \tag{22}$$

where $(\sqrt{(n+\lambda)\cdot(P_{k-1}+Q)})_i$ is the ith row of the matrix square root, and $\lambda = \alpha^2(n+\kappa) - n$, in which α and κ are two scaling parameters. A subtle detail worth noting is that the dimension of covariance P_{k-1} is 6×6, since the degree of freedom (DOF) of the state vector is 6 (the unit quaternion constraint reduces one DOF). Therefore, the ψ_is are 1×6 vectors.

UKF addresses the approximation of a nonlinear system by using a minimal set of sample points, i.e., sigma points, to capture the mean and covariance estimates. The sigma points set $\{(\chi_{k-1})_i\}$ is defined by

$$(\chi_{k-1})_i = \hat{x}_{k-1} = \left[{}^{s}_{E}\hat{\bar{q}}_{k-1},\ {}^{s}\hat{\omega}_{k-1}\right] \tag{23}$$

as $i = 0$, and

$$(\chi_{k-1})_i = \hat{x}_{k-1} + \psi_i = \left[{}^{s}_{E}\hat{\bar{q}}_{k-1} \otimes \exp(\psi_{i|q}),\ {}^{s}\hat{\omega}_{k-1} + \psi_{i|\omega}\right] \tag{24}$$

when $i = 1,\ldots,2n$, and $\psi_i = [\psi_{i|q},\ \psi_{i|\omega}]$ in which $\psi_{i|q}$ is the first three elements of ψ_i corresponding to the quaternion part, and $\psi_{i|\omega}$ relates to the angular velocity. The length of state vector $\hat{x}_{k-1}$ is 7, while ψ_i is a six-element vector. Thereby, equation (24) performs a vector to quaternion conversion for $\psi_{i|q}$ using the quaternion exponential in equation (5).

After the sigma points $\{(\chi_{k-1})_i\}$ are obtained, the process model is used to project each point ahead in time. The propagation results are shown in equation (25), and *a priori* state estimate is thus obtained in equation (26):

$$(\chi_k)_i = f((\chi_{k-1})_i, 0, 0) \qquad \text{for } i = 0,\ldots,2n \tag{25}$$

$$\hat{x}_k^- = \sum_{i=0}^{2n} W_i^{(m)} (\chi_k)_i \tag{26}$$

where weights $W_i^{(m)}$ are defined by

$$W_i^{(m)} = \begin{cases} \lambda/(n+\lambda) & i = 0 \\ \lambda/(2(n+\lambda)) & i = 1,\ldots,2n. \end{cases} \tag{27}$$

The covariance of $(\chi_k)_i$ is

$$P_k^- = \sum_{i=0}^{2n} W_i^{(c)} [(\chi_k)_i - \hat{x}_k^-][(\chi_k)_i - \hat{x}_k^-]^T \tag{28}$$

where weights $W_i^{(c)}$ are defined in equation (29), and β is a scaling parameter used to incorporate prior knowledge about the distribution of state vector x. It should be noted that P_k^- is a 6×6 matrix, while $(\chi_k)_i$ and $\hat{x}_k^-$ are seven-element vectors. A conversion is thereby performed to the right side of the equation to transform the quaternion parts into three-element rotation vectors [51]. This quaternion-to-rotation conversion is a reverse procedure of equation (5):

$$W_i^{(c)} = \begin{cases} \lambda/(n+\lambda) + (1-\alpha^2+\beta) & i = 0 \\ \lambda/(2(n+\lambda)) & i = 1,\ldots,2n. \end{cases} \tag{29}$$

The results for the projected set $\{(\chi_k)_i\}$ in the sensor model are expressed by

$$(\mathbf{y}_k)_i = h((\chi_k)_i, 0, 0) \qquad \text{for } i = 0,\ldots,2n. \tag{30}$$

The measurement estimate can thus be defined in equation (31):

$$\hat{z}_k^- = \sum_{i=0}^{2n} W_i^{(m)} (\mathbf{y}_k)_i. \tag{31}$$

The *a posteriori* state estimate is computed using

$$\hat{x}_k = \hat{x}_k^- + K_k(z_k - \hat{z}_k^-) \tag{32}$$

where z_k is the measurement vector from WIMU, and K_k is the Kalman gain which is defined by

$$K_k = P_{\hat{x}_k\hat{z}_k} P_{\hat{z}_k\hat{z}_k}^{-1}. \tag{33}$$

The cross correlation matrix $P_{\hat{x}_k\hat{z}_k}$ and measurement estimate covariance $P_{\hat{z}_k\hat{z}_k}$ are expressed in equations (34) and (35), respectively:

$$P_{\hat{x}_k\hat{z}_k} = \sum_{i=0}^{2n} W_i^{(c)} [(\chi_k)_i - \hat{x}_k^-]^T [(\mathbf{y}_k)_i - \hat{z}_k^-] \tag{34}$$

$$P_{\hat{z}_k\hat{z}_k} = \sum_{i=0}^{2n} W_i^{(c)} [(\mathbf{y}_k)_i - \hat{z}_k^-]^T [(\mathbf{y}_k)_i - \hat{z}_k^-] + R. \tag{35}$$

A quaternion-to-rotation conversion is performed to the term in the second bracket of equation (34), to ensure a valid cross correlation matrix. The estimated state covariance is updated at instant k by

$$P_k = P_k^- - K_k P_{\hat{z}_k\hat{z}_k} K_k^T. \tag{36}$$

4.5. Initialization and filter parameters

For a successful UKF performance, the following parameters are required to be determined first: Q_k, R, α, β, κ. Scaling parameters α, β, κ are empirically pre-set and given reasonable values based on filter tests results. ${}^{R}\sigma_{\omega}^2\mathbf{I}_{3\times3}$ and ${}^{R}\sigma_{a}^2\mathbf{I}_{3\times3}$ account for the spectral density of the sensor signal while the sensor is lying still.

The process noise covariance Q_k can be determined by

$$Q_k = \Phi_s \int_0^{Ts} \mathbf{\Phi}(\tau) Q' \mathbf{\Phi}^T(\tau)\, \mathrm{d}\tau \tag{37}$$

where Φ_s is a scaling parameter, $\mathbf{\Phi}(\tau)$ is an approximation to the fundamental matrix calculated by taking the Taylor-series expansion of the system dynamic matrix, and Q' is the

continuous process noise matrix [63]. The covariance matrix Q' is expressed by

$$Q' = \begin{bmatrix} \Sigma_q & \mathbf{0} \\ \mathbf{0} & \Sigma_\omega \end{bmatrix} \tag{38}$$

where $\Sigma_q = {}^{Q}\sigma_q^2\mathbf{I}_{3\times3}$ and $\Sigma_\omega = {}^{Q}\sigma_\omega^2\mathbf{I}_{3\times3}$ are the covariance matrix of the quaternion part and angular velocity part of the process noise, respectively, which are assumed to be uncorrelated, zero-mean white noise.

5. Simulations and experiments

5.1. Experimental equipment

The orientation estimation scheme was tested using the WIMU detailed in section 3. Raw data was recorded, transmitted to a desktop, and processed by the proposed scheme. A welding robot (Universal Robot UR 5) was used to provide reference measurements of the torch orientation. To do so, either the torch (in welding experiments) or the WIMU (in simulations) was rigidly mounted on the robot tool center, the center of the plane on the robot forearm [64]. The orientation of the tool center was calculated by the imported accompanying software using the feedback from the robot. The obtained reference orientation was filtered by a second-order low-pass Butterworth filter (cut-off frequency: 15 Hz). Initial calibration was conducted to determine the quaternion for converting the tool center orientation to the torch/WIMU orientation. The performance of the proposed scheme was evaluated by comparing it with the reference measurements.

The accuracy of the reference orientation delivered by the welding robots depends on the accuracy of the orientation measurement of the robot tool center and on the robot-WIMU orientation calibration. The orientation measurement error of the robot can be estimated using the data supplied by the robots manufacturer [64]. The repeatability of the robot is ±0.1 mm. The robot's shortest forearm around which the robot tool center rotates is about 89 mm. Hence, its maximum orientation error is about 0.06°, which is acceptable as a measurement reference for our target applications.

5.2. Simulations procedure

A reference 3D Cartesian coordinate frame ${}^{\mathrm{E}}(XYZ)$ was defined to justify valid orientation measurements: the z-axis has been defined in section 3; the x-axis and y-axis were arbitrarily defined by the right-hand rule. The WIMU was mounted on the robot tool center such that its internal coordinate frame ${}^{s}(XYZ)$ was identical to frame ${}^{\mathrm{E}}(XYZ)$ at the initial position.

To simulate a human hand's behavior, the welding robot was set in the teaching mode such that the robot tool center could be rotated manually and smoothly around the three axes of its internal frame. Four data sets were constructed in simulations denoted by D_i^s, where $i = 1, 2, 3, 4$. To evaluate the performance of the proposed scheme in the three dimensions separately, the WIMU was rotated around one axis in each simulation by the leading author. Hence, for D_1^s to D_3^s, the robot tool center (and the WIMU) was rotated around the x-axis, y-axis and z-axis, respectively. The rotation sequence in the three data sets is identical, i.e., first rotate 90° [5], back to initial position, then rotate -30°, and back to initial position again. In each stage (at 90°, -30° and the initial positions), the robot tool center stayed still for a few seconds. It should be noted that the stationary phases might not exactly be 90°, -30° or 0°, since the robot tool center was manually rotated by the leading author. Yet, it does not affect the simulation procedure, or the estimation accuracy.

For D_4^s, the robot tool center was rotated around the three axes together with the aforementioned rotation sequence. The robot tool center was thought to be much steadier than a human hand due to a human's inherent neuro latency. To this regard, data set D_{4+n}^s was further artificially constructed by introducing two random Gaussian noises into the gyro and acceleration data in D_4^s, respectively, in order to simulate the unsteadiness of a human hand. The variances of the noise for the gyro and acceleration data in D_4^s were 5×10^{-2} and 5×10^{-1}.

Two UKF implementations were studied, henceforth called method A and method B. Method A incorporated the auto-nulling algorithm, while method B did not. Two additional trapezoidal numerical integration methods were also included as two comparisons: method C adopted the auto-nulling algorithm, while method D did not. Four methods were tested at three different sampling rates: 256, 128 and 51.2 Hz. Six repeated tests were conducted for each condition, including both methods and sampling rates.

The performance metric adopted in this study is the root-mean-square error (RMSE_θ) of the orientation in degree, which is defined by

$$\mathrm{RMSE}_\theta = \sqrt{\frac{1}{n}\sum_{k=0}^{n-1}(\triangle\theta_k)^2} \tag{39}$$

where n is the sample number of the data set being evaluated:

$$\triangle\theta_k = \frac{2*180}{\pi}\arccos((q_{t_k}\otimes q_{e_k}^*)_0) \tag{40}$$

where q_{t_k} and q_{e_k} are the truth-reference and estimated quaternion. Besides the RMSE_θ, the RMSEs of rotated Euler angles in three axes were also adopted, denoted by RMSE_x, MRSE_y and RMSE_z, respectively.

5.3. Experimental validation

Two data sets of torch orientation used in this section, denoted by D_1^e and D_2^e, were obtained from welding experiments. The data set D_1^e was collected from the GTAW experiments, containing four types of welding fit-ups sequentially corresponding to the configurations in figure 1, and the data set D_2^e was obtained from the GMAW experiments including the welding types as shown in figure 2. Furthermore, two more data sets D_{1+n}^e and D_{2+n}^e were artificially constructed by introducing the same noise mentioned in the last section into D_1^e and D_2^e, respectively. The tested method was method A, which was the contest winner in the simulation trials. Six repeated trials were conducted for each welding type.

[5] The positive direction indicates a clockwise rotation as viewed from the negative to the positive direction of one axis.

Table 1. Major welding conditions for the GTAW experiments.

Welding parameter	Conditions
Welding current (A)	60
Welding speed (mm s^{-1})	1 ∼ 2 (varied by the welder)
Tungsten tip-to-work distance (mm)	2 ∼ 5 (varied by the welder)
Electrode extension (mm)	3
Electrode type	EWCe-2
Electrode diameter (mm)	2.38
Electrode tip geometry (deg)	30
Shielding gas	Argon 100%
Flow rate of shielding gas (L min^{-1})	11.8
Material	2 mm thick 304 L sheet

To construct the data sets, the WIMU attached torch (as shown figure 3) was mounted on the tool center of the welding robot which was set in the teaching mode. The leading author (a novice welder) was asked to hold the robot forearm and perform the aforementioned experiments. Each welding type lasted about 30 s. The welder took a break and set the torch to the initial posture between every two welding trials. The welding conditions for the GTAW experiments are listed in table 1. No filler metal was used in the experiments. For the GMAW experiments, not only the torch orientations were required to be maintained, but the specific torch swing patterns needed to be followed. In the experiments, the arc did not start due to the limited welding skill of the leading author, i.e., the torch was firmly held above and smoothly dragged along the weld beam without the arc being established. The experimental data was transmitted to a host desktop, and was processed off-line using Matlab R2011.

A reference 3D Cartesian coordinate frame ${}^{\mathsf{E}'}(XYZ)$ was defined for the experimental data. The negative direction of ${}^{\mathsf{E}'}Z$ coincided with the gravitational direction. The positive direction of ${}^{\mathsf{E}'}Y$ was the welding direction along the weld seam. Axis ${}^{\mathsf{E}'}X$ was then determined using the right-hand rule. In the experiments, the spatial relation between the torch and the robot was carefully calibrated. In the initial posture, the torch head was set such that directions of the axis in ${}^{\mathsf{E}'}(XYZ)$ coincide with those in ${}^{t}(XYZ)$, respectively.

6. Results and discussion

6.1. Results

6.1.1. Simulation results. The initial parameters for the UKF are listed in table 2. The mean and standard deviation of the gyro's output when the WIMU is stationary at room temperature conditions, μ_s and σ_s, were measured using equations (41) and (42). The coefficients ρ_μ and ρ_σ were chosen to be 1.0 when conducting the simulations:

$$\mu_s = [8.50 \times 10^{-3} \quad 1.56 \times 10^{-2} \quad 4.70 \times 10^{-3}] \tag{41}$$

$$\sigma_s = [1.18 \times 10^{-4} \quad 1.47 \times 10^{-4} \quad 9.87 \times 10^{-5}]. \tag{42}$$

The statistics of the resultant estimation of the RMSE_θ are listed in table 3. In the table, the estimated performance of the proposed algorithm (method A) is compared with the other three counterpart algorithms by the mean and the standard deviation of the RMSE_θ.

Table 2. Initializations of the UKF parameters for methods A and B.

	${}^{Q}\sigma_q$	${}^{Q}\sigma_\omega$	${}^{R}\sigma_\omega$	${}^{R}\sigma_a$	α	β	κ
Method A	0.18	0.08	0.5	0.2	1.4	1.0	0
Method B	0.27	0.18	1.2	0.4	1.0	0	3.0

The results of the orientation estimation for the three individual axes (RMSE_s [°]) are presented in table 4. The evaluated data sets are D_1^s, D_2^s and D_3^s, respectively.

Figures 4 and 5 show the time functions of the Euler angles as they were measured in the simulation trials, and the reference measurements were from the welding robot. In particular, figure 4 shows the estimation of the orientation in the x-axis, y-axis and z-axis using data sets D_1^s, D_2^s and D_3^s, respectively. The 3D orientation estimation is presented in figure 5, obtained using the four algorithms with data set D_4^s. Figure 6 shows the quaternion time functions obtained by the proposed algorithm, i.e., method A, using the data set corresponding to figure 5. It should be noted that each of the figures only shows one of the estimation result of the six trials for the corresponding simulation conditions.

Tables 3 and 4 show the estimation results of slow torch movement, in which the angular rate is about 3° s^{-1}. The orientation estimation results for an angular rate larger than 5° s^{-1} of the torch movement are presented in table 5.

6.1.2. Experimental results. One can find from the simulation results that the proposed algorithm (method A) produces the best performance. The sampling rate chosen to conduct the experiments is 128 Hz, since it is the best trade-off between estimation accuracy and computation load. Table 6 shows the mean and standard deviation of the estimated RMSE_θ obtained from the aforementioned experiments consisting of the two welding processes (GTAW and GMAW), each of which includes the four welding fit-ups. Since the welding experiments last only about 40 s on average, the ambient temperature is not significantly changed compared with that when the WIMU were tested for the static drift. Therefore, thermal coefficients ρ_μ and ρ_σ were tuned in the range between 1.2 to 2.1 (they were set at 1.0 in the GMAW experiments).

Figures 7–10 show the typical orientation estimation results in Euler angles. In particular, figure 7 shows the estimation results in one GTAW process with a lap joint, corresponding to the welding process shown in figure 1(*B*). The initial posture of the torch should be 0° in all the three axes. According to the related welding type (figure 1(*B*)), the welder is expected to maintain the 3D orientation of the torch at [20°, −20°, CR], where CR denotes 'custom-related', i.e., the orientation in that particular axis depends on the welder's individual operation custom. One can see in figure 7 that the torch orientation deviated about 5° from the recommended torch posture as shown in figure 1(*B*). This is normal since the welder, i.e., the leading author, is a novice welder who has not mastered the torch manipulation yet. The welding processes, the results of which are shown in figures 8–10, are illustrated in figures 2(*A*)–(*C*), respectively. The recommended torch postures for the three welding types

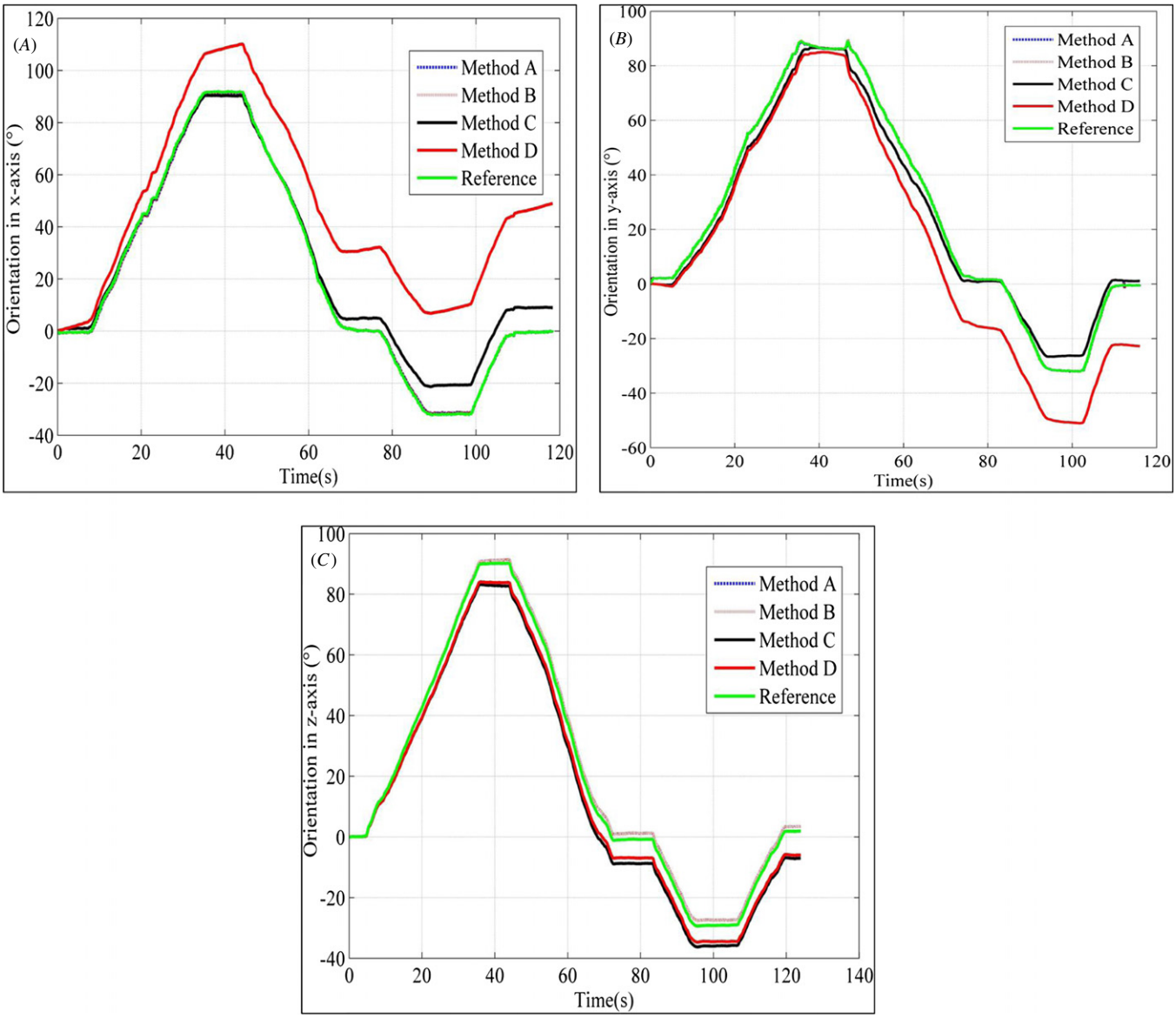

Figure 4. Estimated and reference orientation (in Euler angle) at a sampling rate of $f_s = 128$ Hz for (*A*) the *x*-axis using data set D_1^s, (*B*) the *y*-axis using data set D_2^s, and (*C*) the *z*-axis using data set D_3^s.

Table 3. Orientation estimation (RMSE_θ), in the form of the mean± standard deviation, obtained by the different estimation methods in the course of the Monte Carlo performance trials. The additional distance of gyro and acceleration were artificially introduced in data set D_{4+n}^s.

	D_1^s	D_2^s	D_3^s	D_4^s	D_{4+n}^s
$f_s = 256$ Hz					
A	0.53 ± 0.11	0.47 ± 0.14	0.91 ± 0.20	0.98 ± 0.25	1.35 ± 0.34
B	2.56 ± 0.17	2.74 ± 0.55	1.50 ± 0.48	2.67 ± 0.41	3.02 ± 0.58
C	4.91 ± 0.54	5.11 ± 1.36	6.43 ± 0.81	7.48 ± 0.67	7.85 ± 0.98
D	25.97 ± 2.58	19.18 ± 1.57	21.72 ± 2.27	30.14 ± 3.49	32.56 ± 3.98
$f_s = 128$ Hz					
A	0.50 ± 0.13	0.40 ± 0.16	0.94 ± 0.29	1.01 ± 0.20	1.28 ± 0.32
B	3.52 ± 0.93	2.97 ± 0.73	2.25 ± 0.47	2.21 ± 0.35	2.45 ± 0.47
C	5.27 ± 1.18	6.12 ± 1.57	5.73 ± 0.36	7.14 ± 0.58	8.01 ± 0.79
D	28.39 ± 5.17	23.59 ± 4.18	29.42 ± 1.31	31.30 ± 4.78	41.44 ± 5.36
$f_s = 51.2$ Hz					
A	0.67 ± 0.03	0.52 ± 0.08	1.57 ± 0.32	2.59 ± 0.24	2.81 ± 0.22
B	2.21 ± 0.28	3.74 ± 0.42	3.17 ± 0.52	3.75 ± 0.27	4.11 ± 0.31
C	5.45 ± 1.71	7.94 ± 3.84	8.49 ± 3.67	9.42 ± 3.65	9.84 ± 4.22
D	19.64 ± 3.82	18.12 ± 2.57	23.44 ± 5.12	25.14 ± 4.25	27.51 ± 4.44

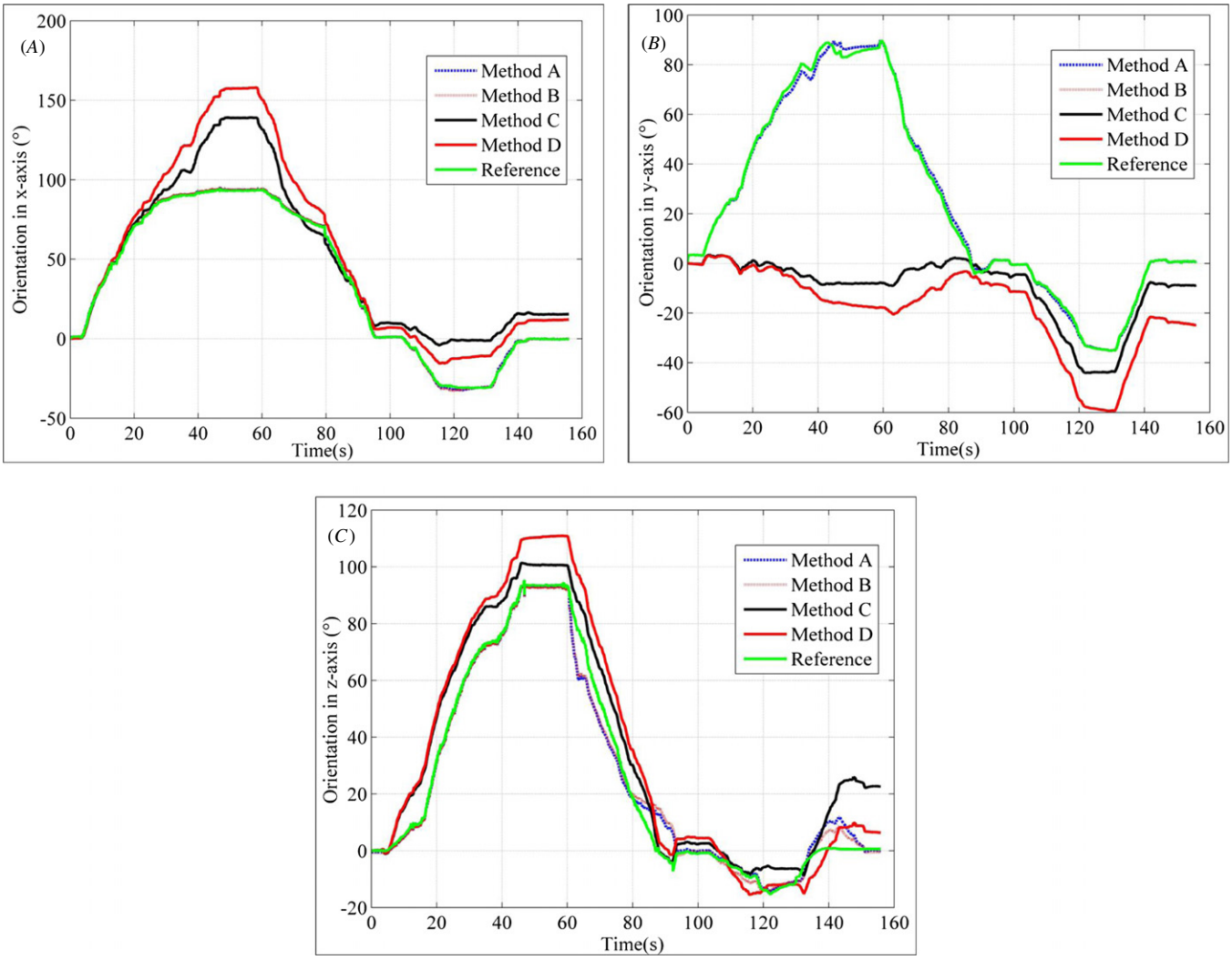

Figure 5. The RMSEs of orientation in the Euler angle at a sample rate of $f_s = 51.2$ Hz for (*A*) RMSE$_x$, (*B*) RMSE$_y$ and (*C*) RMSE$_z$ using data set D_4^s.

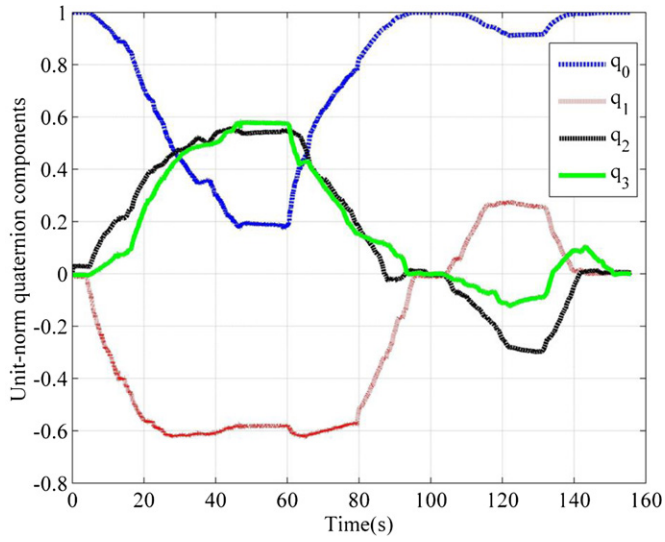

Figure 6. The obtained unit-norm quaternion of rotation from data set D_4^s using method A at a sampling rate $f_s = 51.2$ Hz. The quaternion components are dimensionless.

Table 4. Orientation estimation (RMSEs (°)), in the form of mean ± standard deviation, obtained by the different estimation methods in the course of six repeated trials for each simulation.

	D_1^s	D_2^s	D_3^s
$f_s = 256$ Hz	RMSE$_x$	RMSE$_y$	RMSE$_z$
A	0.23 ± 0.01	0.16 ± 0.01	0.49 ± 0.04
B	0.26 ± 0.05	0.46 ± 0.29	1.14 ± 0.37
C	4.77 ± 0.58	4.60 ± 1.25	4.97 ± 0.71
D	12.86 ± 2.55	10.62 ± 1.30	13.42 ± 2.10
$f_s = 128$ Hz			
A	0.32 ± 0.02	0.25 ± 0.02	0.76 ± 0.14
B	0.34 ± 0.02	0.70 ± 0.03	1.72 ± 0.31
C	4.69 ± 0.69	4.34 ± 0.94	5.16 ± 0.23
D	15.39 ± 2.58	10.86 ± 2.46	20.34 ± 1.51
$f_s = 51.2$ Hz			
A	0.60 ± 0.02	0.46 ± 0.05	0.81 ± 0.18
B	0.62 ± 0.02	0.49 ± 0.05	2.24 ± 0.41
C	4.99 ± 1.39	6.68 ± 3.21	7.16 ± 2.33
D	10.97 ± 8.22	9.95 ± 1.64	24.79 ± 3.10

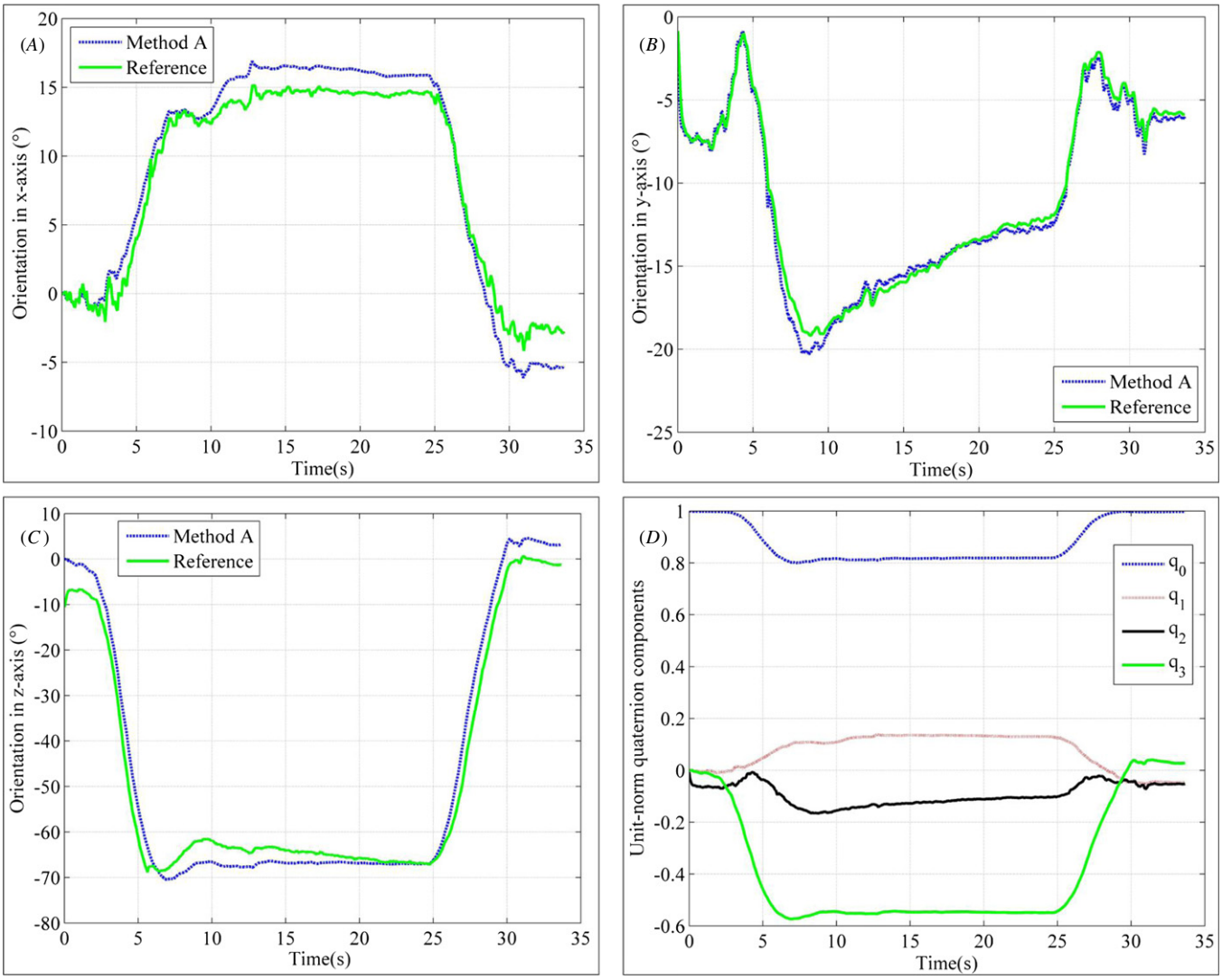

Figure 7. Orientation estimations in (*A*) the *x*-axis, (*B*) the *y*-axis and (*C*) the *z*-axis, and (*D*) the unit-norm quaternion components in a GTAW experiment using the proposed estimation algorithm, i.e., method A. The used data set is D_1^e. The weld type is a lap joint corresponding to figure 1(*B*).

Table 5. Dynamic Orientation estimation [RMSE$_\theta$](°), in the form of mean± standard deviation, obtained by method A. The angular rate is larger than 5°.

	$f_s = 51.2$	$f_s = 128$	$f_s = 256$
D_1^s	1.40 ± 0.06	0.89 ± 0.18	0.61 ± 0.08
D_2^s	1.74 ± 0.07	0.91 ± 0.19	0.54 ± 0.11
D_3^s	1.89 ± 0.28	1.25 ± 0.35	1.10 ± 0.38
D_4^s	3.28 ± 0.29	1.62 ± 0.35	1.25 ± 0.26
D_{4+n}^s	3.56 ± 0.45	1.94 ± 0.41	1.55 ± 0.35

Table 6. Orientation estimation [RMSE$_\theta$](°), produced by different data sets using method A with a sampling rate of $f_s = 128$ Hz. The four types of welding account for those in figure 1 (for data set D_1^e and D_{1+n}^e), and in figure 2 (for data set D_2^e and D_{2+n}^e).

	Type A	Type B	Type C	Type D
D_1^e	2.59 ± 0.37	3.10 ± 0.44	2.67 ± 0.46	2.78 ± 0.42
D_2^e	2.37 ± 0.42	2.11 ± 0.59	2.14 ± 0.35	3.40 ± 0.54
D_{1+n}^e	3.74 ± 0.51	3.46 ± 0.45	3.44 ± 0.45	3.32 ± 0.48
D_{2+n}^e	4.04 ± 0.31	3.57 ± 0.41	3.84 ± 0.39	3.62 ± 0.51

are [10° ∼ 20°, −45°, CR], [80°, 0°, 0°], and [100°, 0°, 0°], respectively. Similarly, the orientation deviations from the corresponding recommendations are observed in the resultant figures. Nevertheless, those deviations do not affect the estimation accuracy of the proposed algorithm.

6.2. Discussion

In the proposed measurement, i.e., method A, the auto-nulling algorithm is incorporated in the effort to compensate the possible time-varying gyro drift during the simulations and the welding experiments; while for the in-line self-calibration of the accelerometer, multiple postures are required. However, the torch orientation is expected to be maintained at the recommended postures throughout the welding experiments. There are thus not enough postures in a single experiment for the accelerometer to conduct the calibration.

The UKF parameter initialization listed in table 2 is found to work well after running an extensive number of simulations

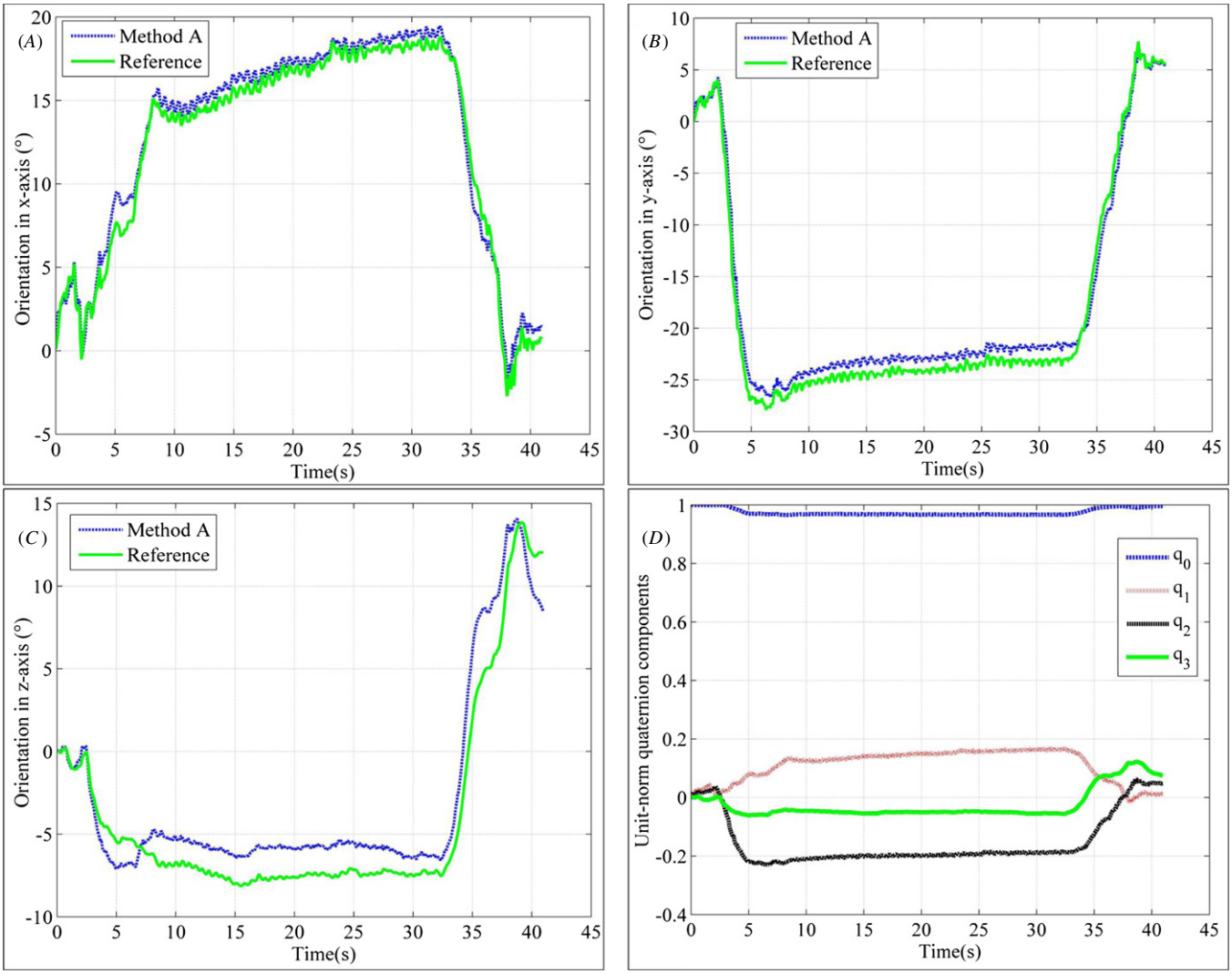

Figure 8. Orientation estimations in (*A*) the *x*-axis, (*B*) the *y*-axis and (*C*) the *z*-axis, and (*D*) the unit-norm quaternion components in a GMAW experiment using the proposed estimation algorithm, i.e., method A. The used data set is D_2^e. The weld type is a horizontal–vertical fillet corresponding to figure 2(*A*).

or experiments, even in the presence of the incorporated noises. The WIMU was calibrated well before use. In addition, the auto-nulling algorithm was also incorporated in method A to compensate for the gyro drift. Hence the covariances of the measurement noise and the process noise chosen for method A are comparatively small; while the covariances in method B are selected to be larger than those in A due to the absence of the auto-nulling algorithm. It is expected that increasing the process noise should be able to compensate for the disturbance of the inaccurate modeling and to improve the tracking ability of the filter.

The results reported in tables 3 and 4 show that the combination of the UKF and the auto-nulling algorithm give the best performance. Results for the *x*-axis and *y*-axis orientation estimations are comparable in accuracy. Yet, the *z*-axis estimation shows comparatively poor accuracy. It is arguable that because the accelerometer cannot provide the torch's orientation information in the *z*-axis, estimations in the UKF solely rely on the accuracy of the gyro outputs themselves. The performance is thus relatively poor without aid from the acceleration data. Another interesting observation can be found in table 4 by comparing the performance of method A and method B: the RMSE_xs and RMSE_ys yielded by the two methods are comparable, yet, the corresponding RMSE_θ obtained using method A is significantly smaller. One can conclude from this observation: (1) the main source of RMSE_θ is from the estimation for the *z*-axis (heading); (2) significant improvement in estimation accuracy can be obtained by applying the proposed auto-nulling algorithm to compensate for the gyro drift.

Data from a magnetic sensor could be fused into the UKF to improve the estimation accuracy in the *z*-axis. However, with the existence of the strong magnetic interference from the welding machine and welding arc, the accuracy of the orientation estimation may not be guaranteed. Thus, incorporating an additional magnetic sensor, it might not be a good choice for applications in the welding fields. Fortunately, even without an extra magnetic sensor, the 3D

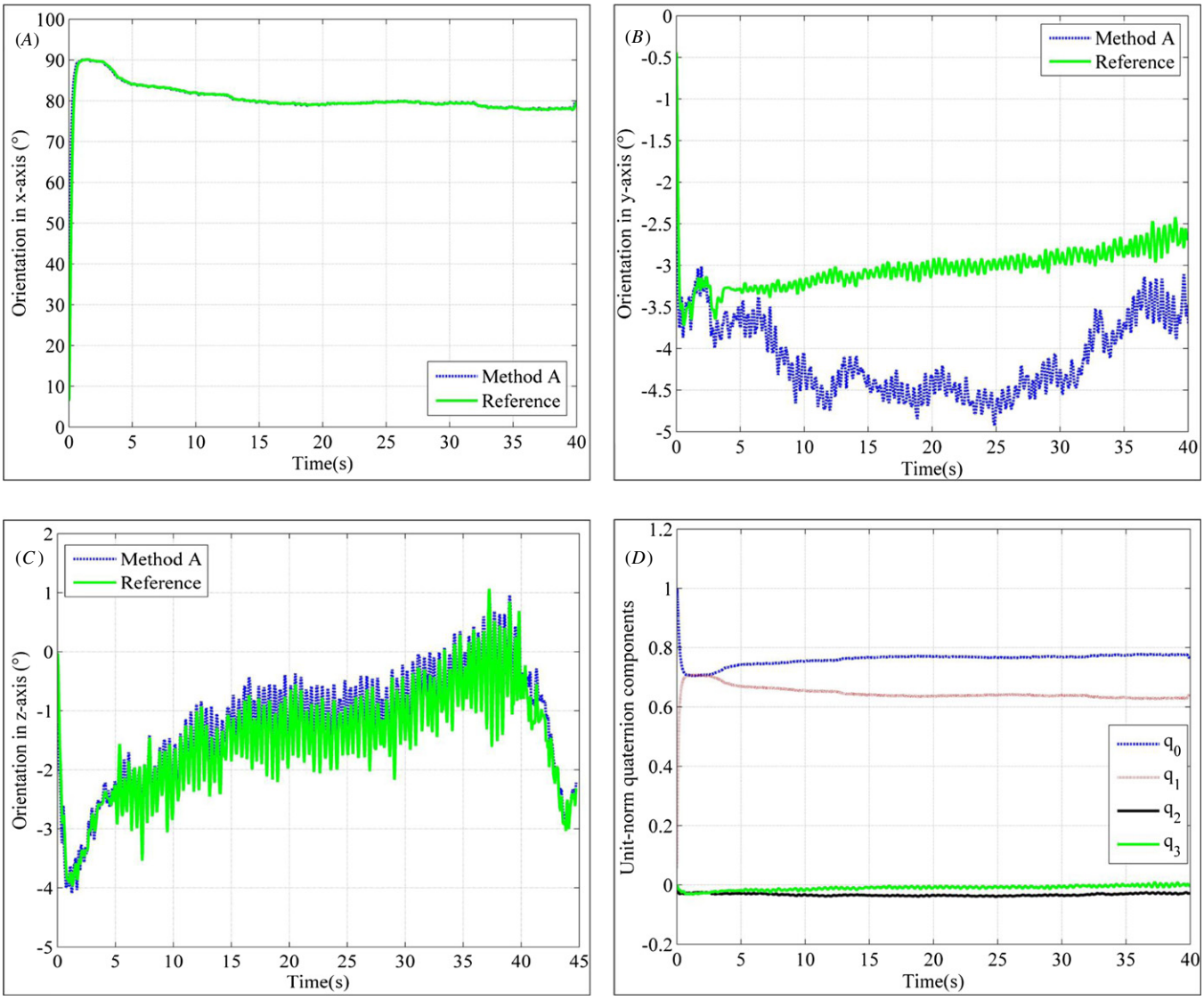

Figure 9. Orientation estimations in (*A*) the *x*-axis, (*B*) the *y*-axis and (*C*) the *z*-axis, and (*D*) the unit-norm quaternion components in one GMAW experiment using the proposed estimation algorithm, i.e., method A. The used data set is D_2^e. The weld type is a vertical up root pass corresponding to figure 2(*B*).

estimation errors reported in tables 3 and 6 are acceptable compared with state-of-art research in other academic communities [30, 35, 38]. Furthermore, only accelerometers and gyroscopes are applied in the proposed method, while other methods added magnetometers.

Degradations in estimation accuracy are observed in both tables 3 and 6 after injecting the noise into the gyro data and acceleration data. The auto-nulling algorithm should be able to compensate for the noise in the gyro data. However, the contaminated acceleration data contains both the gravitation and the fake acceleration induced by the injected noise, while the acceleration of the WIMU is considered as a disturbance in the sensor model (equation (8)). The sensor model thus tends to be less accurate with the existence of the acceleration, and that leads to a degraded orientation estimation. Similar results can be found in table 5. As the torch movement becomes faster, the accelerometer is more likely to detect the acceleration of the torch's movement. The estimation accuracy is thus degraded.

Within the limits of our analysis, increasing the sampling rate does improve the estimation accuracy, but its effect is not prominent. Unlike the EKF, which usually requires a high sampling rate to avoid the possible filter instability, the UKF has no such stability issue. Increasing the sampling rate is a huge computation and energy assumption burden for the battery-powered WIMU. Therefore, the sampling rate was set at 128 Hz in the welding experiments.

One can find that some of the recommended torch orientations do not require specifications for the *z*-axis posture, such as those for the welding types in figure 1. This is because the torch posture in the *z*-axis does not necessarily relate to weld quality in some welding processes. On the other hand, a proper *z*-axis torch posture is recommended for weld types like those shown in figure 2, in order to perform a qualified weld. Furthermore, in the applications mentioned in section 1, an accurate totally 3D orientation estimation might be highly appreciated.

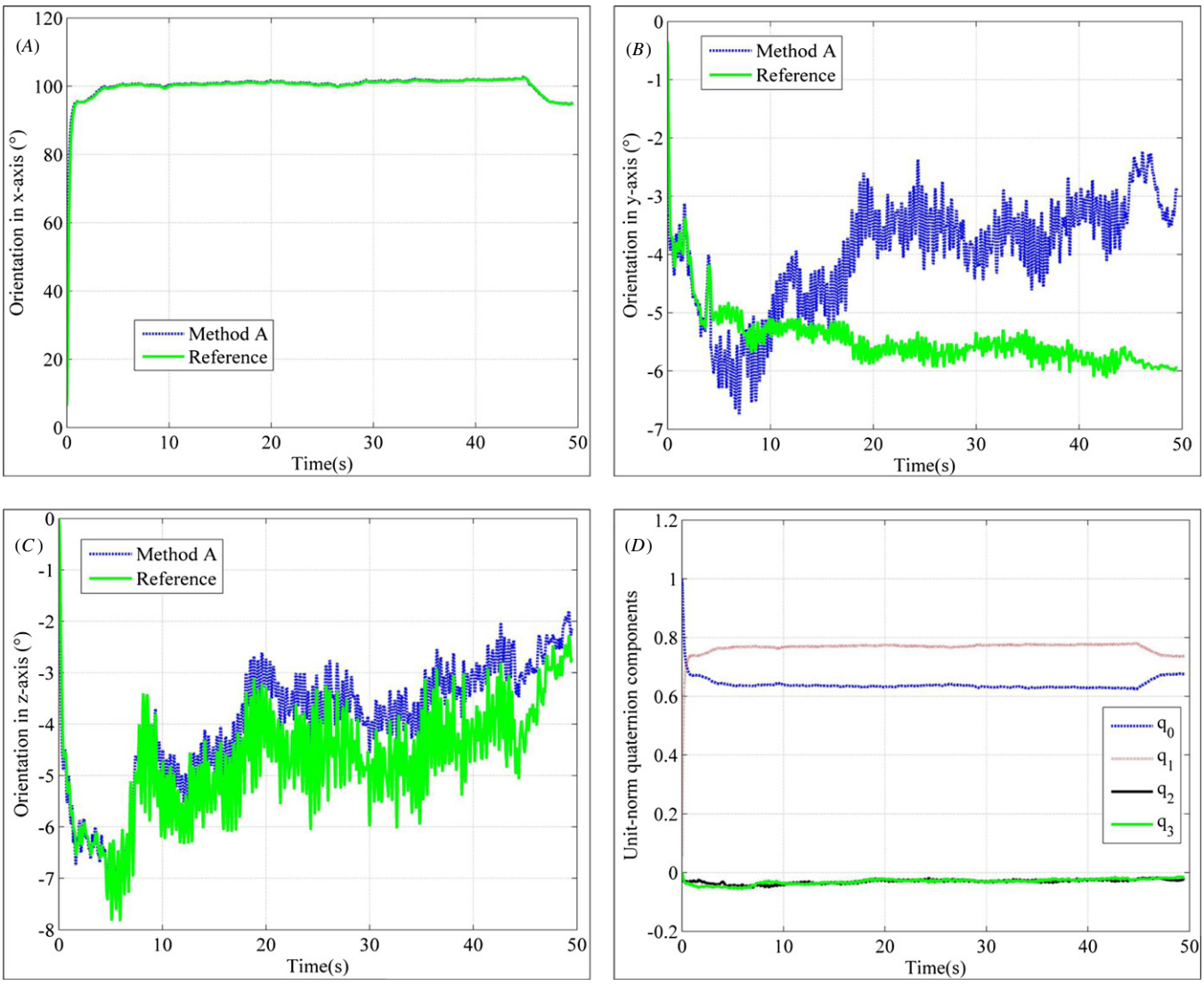

Figure 10. Orientation estimations in (*A*) the *x*-axis, (*B*) the *y*-axis and (*C*) the *z*-axis, and (*D*) the unit-norm quaternion components in a GMAW experiment using the proposed estimation algorithm, i.e., method A. The used data set is D_2^e. The weld type is a vertical up root pass corresponding to figure 2(*C*).

The effect of the torch's swing motions to the torch orientation can be found by comparing figure 7 and figures 8–10: more ripples are observed in the torch orientation curves as torch swing motions are augmented. Yet, in this study, no extra errors were observed to be yielded in the orientation estimation due to the swing motions.

7. Conclusion and future work

An innovative measurement scheme for the 3D welding torch orientation, which can be conveniently adapted into a manual arc welding process or a welder training system, is developed in this paper. The proposed measurement scheme is composed of a quaternion-based UKF incorporated by an auto-nulling algorithm. The UKF aims for the estimation of the 3D welding torch orientation using a miniature WIMU endowed with a tri-axis gyro and a tri-axis accelerometer. The auto-nulling algorithm serves as an in-line calibration procedure to compensate for the gyro drift, which has been verified to significantly improve the estimation accuracy in three-dimensions, especially in the heading estimation. It has been found that the proposed scheme is able to provide an accurate orientation estimation without aid from an extra magnetometer. The accuracy of the estimation using the proposed scheme has been validated by simulation and welding experiments. Statistics show that the estimation error in welding experiments is in the order of 3°.

The future work of the authors is to incorporate the WIMU along with the proposed UKF in a manual welding process such that the welder's torch manipulations can be recorded, studied and modeled in relation to weld quality characters, such as the weld beam appearance and the weld penetration depth.

Acknowledgments

This work is funded by the National Science Foundation under grant CMMI-0927707.

References

[1] Raj B, Jayakumar T and Thavasimuthu M 2002 *Practical Non-destructive Testing* (Cambridge: Woodhead Publishing)

[2] Rampaul H 2003 *Pipe Welding Procedures* 2nd edn (South Norwalk, CT: Industrial Press)

[3] Moreno P 2013 *Welding Defects* 1st edn (Rome: Aracne)

[4] AWS 2003 Recommended practices for gas tungsten arc welding Aws c5.5/c5.5m (Miami, FL: American Welding Society)

[5] AWS 2004 Recommended practices for gas metal arc welding Aws c5.6 (Miami, FL: American Welding Society)

[6] Lincoln Electric 1997 *Lincolns MIG Welding Guidance* (Cleveland, OH: Lincoln Electric)

[7] ESAB 2011 *Welder Guide Book* (Florence, SC: ESAB)

[8] Miller Electric Manufacturing Co. 2003 *Guidelines to Gas Tungsten Arc Welding (GTAW)* (Appleton, WI: Miller Electric)

[9] Miller Electric Manufacturing Co. 2013 *TIG Welding Tips* (Appleton, WI: Miller Electric)

[10] Weman K 2003 *Welding Processes Handbook* (New York: CRC Press)

[11] Lincoln Electric 2012 *VRTEX 360* im10046-e edition (Cleveland, OH: Lincoln Electric)

[12] Teeravarunyou S and Poopatb B 2009 Computer based welding training system *Int. J. Indust. Eng.* **16** 116–25

[13] Zhang W J, Liu Y K and Zhang Yu M 2012 Characterization of three-dimensional weld pool surface in GTAW *Weld. J.* **91** 195s–203s

[14] Zhang W J and Zhang Yu M 2012 Modeling of human welder response to 3d weld pool surface: part I. Principles *Weld. J.* **91** 310s–8s

[15] Zhang W J and Zhang Yu M 2012 Modeling of human welder response to 3d weld pool surface: part II. Results and analysis *Weld. J.* 329s–53s

[16] Zhang W J and Zhang Yu M 2013 Dynamic control of GTAW process using human welder response model *Weld. J.* **92** 154s–66s

[17] Iran T P, Chung T L, Kim H K, Kim S B and Oh M S 2004 Trajectory tracking of mobile manipulator for welding task using sliding mode control *IECON: 30th Annu. Conf. IEEE Industrial Electronics Society* vol 1 pp 407–12

[18] Baea K Y, Leea T H and Ahnb K C 2002 An optical sensing system for seam tracking and weld pool control in gas metal arc welding of steel pipe *J. Mater. Process. Technol.* **120** 458–65

[19] Jeon Y B, Kam B Oh, Park S S and Kim S B 2001 Seam tracking and welding speed control of mobile robot for lattice type welding *ISIE: IEEE Int. Symp. on Industrial Electronics* vol 2 pp 857–62

[20] Shen H, Lin T, Chen S and Laiping Li 2010 Real-time seam tracking technology of welding robot with visual sensing *J. Intell. Robot. Syst.* **59** 283–98

[21] Zhou L, Wang J F, Lin T and Chen S B 2007 Planning the torch orientation of planar lap joint in robotic welding *Robot. Weld. Intell. Autom.* **362** 145–51

[22] Li X, Lu Y and Zhang Y M 2013 Accelerometer-based position and speed sensing for manual pipe welding process *Int. J. Adv. Manuf. Technol.* **69** 705–13

[23] Fast K, Gifford T and Yancey R 2004 Virtual training for welding *Proc. 3rd IEEE and ACM int. Symp. on Mixed and Augmented Reality (Washington, DC)* pp 298–9

[24] RealWeld System 2013 www.realweldsystems.com

[25] Chambers T L, Aglawe A, Reiners D, White S, Borst C W, Prachyabrued M and Bajpayee A 2012 Real-time simulation for a virtual reality-based MIG welding training system *Virtual Real.* **16** 45–55

[26] Kingston D B and Beard R W 2004 Real-time attitude and position estimation for small UAVs using low-cost sensors *Proc. 3rd American Institute of Aeronautics and Astronautics Technical Conf. (Chicago, IL, USA)* pp 20–3

[27] Dongwon J and Panagiotis T 2007 Inertial attitude and position reference system development for a small UAV *Proc. American Institute of Aeronautics and Astronautics Technical Conf. (Rohnert Park, CA, 7–10 May)* paper 07-2763

[28] Beauregard S 2007 Omnidirectional pedestrian navigation for first responders *WPNC: Proc. 4th Workshop on Positioning, Navigation and Communication* pp 33–36

[29] Syed Z F, Aggarwl P, Goodall C, Niu W and El-Sheimi N 2007 A new multi-position calibration method for MEMS inertial navigation systems *Meas. Sci. Technol.* **18** 1897–907

[30] Weenk D, van Beijnum B J F, Baten C T M, Hermens H J and Veltink P H 2013 Automatic identification of inertial sensor placement on human body segments during walking *J. NeuroEng. Rehabil.* **10** 1–9

[31] Zhou H and Hu H 2008 Human motion tracking for rehabilitation—a survey *Biomed. Signal Process. Control* **3** 1–18

[32] Lee H-J and Jung S 2009 Gyro sensor drift compensation by Kalman filter to control a mobile inverted pendulum robot system *ICIT: IEEE Int. Conf. on Industrial Technology* pp 1–6

[33] Verplaetse C 1996 Inertial proprioceptive devices: self-motion-sensing toys and tools *IBM Syst. J.* **35** 639–50

[34] van Heeren H, Bouchaud J, Dixon R and Salomon P 2007 Rewards and risks of moving into new applications case study accelerometers *MST News* **1** 35–9

[35] Luinge H J and Veltink P H 2004 Inclination measurement of human movement using a 3-d accelerometer with autocalibration *IEEE Trans. Neural Syst. Rehabil. Eng.* **12** 112–21

[36] Bortz J E 1971 A new mathematical formulation for strapdown inertial navigation *IEEE Aerospace Electron. Syst.* **7** 61–6

[37] Ignagni M B 1990 Optimal strapdown attitude integration algorithms *J. Guid. Control Dyn.* **13** 363–9

[38] Sabatini A M 2006 Inertial sensing in biomechanics: a survey of computational techniques bridging motion analysis and personal navigation *Computational Intelligence for Movement Sciences: Neural Networks and Other Emerging Techniques* (London: Idea Group Publishing) pp 70–100

[39] Kortier H G, Schepers H M, Sluiter V I and Veltink P H 2013 Estimation of hand and finger kinematics using inertial sensors *4th Dutch Bio-Medical Engineering Conf. (Egmond aan Zee, Netherlands)* pp 24–5

[40] Xsens Technology 2009 *MTi and MTx User Manual and Technical Documentation* (Enschede: Xsens Technology BV)

[41] MicroStrain Inc. 2009 *3DM-GX3-25 Miniature Attitude Heading Reference Sensor* (Williston, VT: MicroStrain)

[42] InterSense Inc. 2008 *InertialCube2+ Manual* 1.0 edition (Bedford, MA: InterSense)

[43] Marins J L, Yun X, Bachmann E R, McGhee R B and Zyda M J 2001 An extended Kalman filter for quaternion-based orientation estimation using MARG sensors *IEEE/RSJ Int. Conf. on Intelligent Robots and System* vol 4 pp 2003–11

[44] Schepers H M, Roetenberg D and Veltink P H 2010 Ambulatory human motion tracking by fusion of inertial and magnetic sensing with adaptive actuation *Med. Biol. Eng. Comput.* **48** 27–37

[45] Wang M, Yang Y, Hatch R R and Zhang Y 2004 Adaptive filter for a miniature MEMS based attitude and heading reference system *Position Location and Navigation Symp.* pp 193–200

[46] Caruso M J 2000 Applications of magnetic sensors for low cost compass systems *IEEE Position Location and Navigation Symp.* pp 177–84
[47] Roetenberg D, Luinge H J, Baten C T M and Veltink P H 2005 Compensation of magnetic disturbances improves inertial and magnetic sensing of human body segment orientation *IEEE Trans. Neural Syst. Rehabil. Eng.* **12** 395–405
[48] Anderson T R 2000 Control of electromagnetic interference from arc and electron beam welding by controlling the physical parameters in arc or electron beam theoretical model *IEEE Int. Symp. on Electromagnetic Compatibility (Washington, DC, Aug.)* vol 2 pp 695–8
[49] Bhieh N, Elsghier E, Khalifa M A and Elamari M S 2007 Controlling arc welding risk to persons with pacemaker *Int. J. Sci. Tech. Autom. Control Comput. Eng.* **1** 213–25
[50] Chou J C K 1992 Quaternion kinematic and dynamic differential equations *IEEE Trans. Robot. Autom.* **8** 53–64
[51] Kraft E 2003 A quaternion-based unscented Kalman filter for orientation tracking *Proc. 6th Int. Conf. of Information Fusion* pp 47–54
[52] Pourtakdoust S H and Asl H G 2007 An adaptive unscented Kalman filter for quaternion-based orientation estimation in low-cost AHRS *Aircr. Eng. Aerosp. Technol.* **79** 485–93
[53] Huyghe B, Doutreloigne J and Vanfleteren J 2009 3d orientation tracking based on unscented Kalman filtering of accelerometer and magnetometer data *IEEE Sensors Applications Symp.* pp 148–52
[54] Wan E A and Van der Merwe R 2000 The unscented Kalman filter for nonlinear estimation *IEEE Adaptive Systems for Signal Processing, Communications, and Control Symp.* pp 153–8
[55] LaViola J J 2003 A comparison of unscented and extended Kalman filtering for estimating quaternion motion *Proc. American Control Conf.* pp 2435–40
[56] Ferraris F, Grimaldi U and Pavis M 1995 Procedure for effortless in-field. Calibration of three-axis rate gyros and accelerometers *Sensors Mater.* **7** 311–30
[57] De Pasquale G and Soma A 2010 Reliability testing procedure for MEMS IMUS applied to vibrating environments *Sensors* **10** 456–74
[58] Tee K S, Awad M, Dehghani A, Moser D and Zahedi S 2011 Triaxial accelerometer static calibration *Proc. World Congress on Engineering (London, UK)* vol 3
[59] MEMSense μIMU and nIMU temperature dependant bias, scale factor and cross sensitivity correction performance revision 1 *Technical Report* 7
[60] Williamson R and Andrews B J 2001 Detecting absolute human knee angle and angular velocity using accelerometer and rate gyroscope *Med. Biol. Eng. Comput.* **39** 294–302
[61] Sabatini A M, Martelloni C, Scapellato S and Cavallo F 2005 Assessment of walking features from foot inertial sensing *IEEE Trans. Biomed. Eng.* **52** 486–94
[62] Hao Y, Hongwei Mu and Liu X 2012 On-line calibration technology for SINS/CNS based on MPF-KF *ICMA: Int. Conf. on Mechatronics and Automation* pp 1132–6
[63] Zarchan P and Musoff H 2009 *Fundamentals of Kalman Filtering: A Practical Approach* (Reston, VA: American Institute of Aeronautics and Astronautics)
[64] Universal Robots 2013 www.universal-robots.com